Communication

Wideband RCS Reduction of Dual-Band Fabry–Perot Cavity Antenna Using Pancharatnam–Berry Phase Coding Metasurface and AMC Surface

Lei Xu, Yufeng Liu, and Wenmei Zhang

***Abstract*—In this communication, we propose a dual-band Fabry–Perot (F–P) cavity antenna with a wideband low radar cross section (RCS) by integrating a Pancharatnam–Berry phase coding metasurface (PBPCM) and artificial magnetic conductor (AMC) surfaces. This antenna comprises two partially reflective surfaces (PRSs) that form two nested F–P cavities for signals in two bands. To reduce the monostatic RCS at high frequencies, a PBPCM is placed on the top side of the upper PRS, leveraging its ability to redirect reflected waves into different directions by encoding the phase on the metasurface. Additionally, two AMC surfaces etched on the top side of both the lower PRS and the ground plane further reduce the low-frequency RCS through phase cancellation. The overall antenna profile is also minimized, owing to the AMC's flexible phase adjustment. The simulated and measured results verify the feasibility of the proposed method. The prototyped F–P cavity antenna exhibits a measured −10 dB impedance bandwidth of 4.15–4.8 and 7.8–8.4 GHz, with peak gains of 10 dBi at 4.45 GHz and 15.9 dBi at 8.3 GHz, respectively. Moreover, a wideband RCS-reduction bandwidth from 3 to 16 GHz is achieved under both *x*- and *y*-polarizations.**

***Index Terms*—Artificial magnetic conductor (AMC), Fabry–Perot (F–P) cavity antenna, Pancharatnam–Berry phase coding metasurface (PBPCM), radar cross section (RCS).**

I. Introduction

The Fabry–Perot (F–P) cavity antenna is renowned for its high directivity and feeding mechanism, making it a crucial component in sensing systems [1], [2], base station communications [3], satellite communications [4], and stealth technology [5]. It comprises a partially reflective surface (PRS), primary radiator, and metallic ground plane, featuring an extremely simple configuration and low manufacturing cost [6], [7], [8]. With advancements in 2-D printing technology, frequency selective surfaces (FSSs) have emerged as a PRS in F–P cavity antenna design. This has led to the exploration of F–P cavity antennas in various characteristics, such as wideband [9], [10], circular polarization [11], [12], [13], reconfigurability [14], [15], [16], dual-band performance [17], [18], [19], [20], and low radar cross section (RCS) [5]. Especially, F–P cavity antennas with low RCS and high gain over a wideband has been widely concerned, driven by the stealth demands in militarily.

Several types of FSSs have been developed to realize diverse frequency bands for F–P cavity antennas [17], [18], [19], [20]. In [17], the F–P cavity antenna with one superstrate layer operates at two bands by generating reflection phases of positive gradient across different frequency bands of FSS. In [19], a dual-band shared-aperture F–P cavity antenna using two FSS layers could operate at 3.45 and 5 GHz. This method of placing multiple layers above the radiator helps to simplify the design of FSSs. However, the profile height will increase as a result.

Additionally, various methods have been employed to reduce the RCS of F–P cavity antenna [5], [21], [22], [23], [24], [25], [26], [27], [28], [29]. By coating an absorbing surface on the PRS, the incident waves can be effectively absorbed, and the enhanced gain can compensate for reduction in directivity integrated by the absorbing surface [21]. Besides, the low-scattering surface, including phase gradient metasurface [22], reconfigurable metasurface [23], [24], [25], [26], polarization conversion metasurface [27], chessboard arrangement metasurface [28], coding metasurface [29], was integrated with the PRS to achieve the optimal radiation and scattering performance. Based on the above solutions, designs for low RCS F–P cavity antenna with circular polarization [30], [31], frequency reconfiguration [32], and switched beams [33] were reported.

So far, many excellent works have been achieved in F–P cavity antennas with low RCS. But we find that most of them operate in a single band and have a high profile. How to implement a multiband F–P cavity antenna with wideband RCS reduction in a low profile is still a challenge.

In this communication, a high gain F–P cavity antenna with wideband RCS reduction and dual working bands is proposed. The primary contribution of this work lies in the merged phase cancellation design of Pancharatnam–Berry phase coding metasurface (PBPCM) [34], [35] and two-layer artificial magnetic conductor (AMC) surfaces to realize wideband RCS reduction. This scheme achieves the compatibility of high gain with low RCS performance in a dual-band design. In particular, the two AMC surfaces minimize the total reflected electric field, thereby reducing RCS in the lower frequency band. Also, they help to cut down the profile of the antenna. This approach provides a new technological path for the design of high-performance stealth antennas by assembling multilayer structures (PBPCM, PRS, and AMC).

II. Working Mechanism of the Proposed Antenna

The schematic of the proposed F–P cavity antenna is shown in Fig. 1(a). A dual-band microstrip antenna, placed at the bottom reflector, serves as the feeding source. The AMC unit cells are arranged around the patch of the feeding source and replace the initial ground in order to reduce the cavity height to a quarter of the wavelength. Two FSSs (FSS1 and FSS2) positioned above the feed antenna act as PRSs to form two resonant cavities at 4.3 and 8.1 GHz. At the higher frequency, FSS1 exhibits partially reflective characteristics, while FSS2 maintains high transmission. Conversely, at the lower frequency, FSS2 demonstrates partial reflection, while FSS1 remains highly transmissive. Additionally, the AMC unit cells are printed on the upper layer of the FSS2 and form the AMC-FSS2 structure. Finally, PBPCM is etched to reduce the RCS.

For the low-frequency signal, the F–P cavity is formed by the FSS2-air layer with a height of h_2. While at high frequency, the F–P cavity is constructed by the FSS1, air layer with a height of h_1

Received 21 June 2024; revised 4 January 2025; accepted 27 January 2025. Date of publication 3 March 2025; date of current version 4 June 2025. This work was supported by the National Natural Science Foundation of China under Grant 62071282. *(Corresponding author: Yufeng Liu.)*

The authors are with the School of Physics and Electronic Engineering, and Shanxi Key Laboratory of Wireless Communication and Detection, Shanxi University, Taiyuan, Shanxi 030006, China (e-mail: liuyufeng@sxu.edu.cn).

Digital Object Identifier 10.1109/TAP.2025.3545650

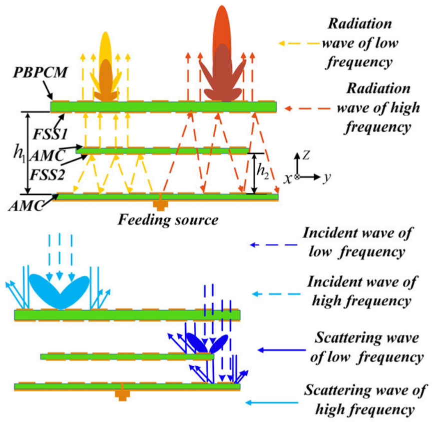

Fig. 1. Schematic model of the F–P cavity antenna. (a) Radiation. (b) Scattering.

and AMC. h_1 and h_2 can be determined according to the resonant condition [6]. That is,

$$h_{1,2} = \frac{\varphi_{\mathrm{PRS}} + \varphi_{\mathrm{GND}}}{2\pi}\frac{\lambda}{2} + N\frac{\lambda}{2}, \quad N = 0, 1, 2, \ldots \tag{1}$$

where φ_{PRS} and φ_{GND} are the reflection phases of the PRS and the ground plane for two frequencies. N is the resonance mode number (N corresponding to h_1 and h_2 are 0 and 2, respectively) and λ represents the wavelength at two working frequencies.

The RCS reduction mechanism is illustrated in Fig. 1(b). At high frequencies, RCS reduction is achieved by the PBPCM. The PBPCM on the top of FSS1, featuring varied reflective phases, redirects scattering beams away from critical angles, thereby diminishing the scattering energy in the normal direction. For low-frequency RCS reduction, a strategy employing dual-layered AMC surfaces is utilized for phase cancellation. According to (1), h_1 is adjusted to $\lambda/2$ when φ_{PRS} and φ_{GND} are set to 180° at 4.3 GHz. Here, the AMC unit cells, with $\varphi_{\mathrm{GND}} = 0°$, are arranged. In this case, h_1 can be minimized to $\lambda/4$. Additionally, when incident waves at 4.3 GHz pass through the FSS1 and into the low-frequency cavity interface, the scattering waves are divided into two components. The first component is reflected by the AMC-FSS2 layer, while the second is reflected by the AMC plane. Due to the $\lambda/4$ cavity and the AMC ground plane, the second component of the waves propagates additional distances of $\lambda/2$ compared with the first component. Thus, there is a 180° phase difference between the two scattering wave components, leading to the RCS reduction.

III. Antenna Configuration for High-Frequency Bands

A. Design and Analysis of PBPCM-FSS1 Structure

As illustrated in Fig. 2(a), the PBPCM-FSS1 structure consists of two metal layers distributed on both sides of the dielectric substrate with a thickness of 4 mm and a relative permittivity of 2.65. The upper layer, shown in Fig. 2(b), is composed of anisotropic metal patterns that are symmetrical about the u-axis. It is referred to as the unit cell of PBPCM. According to the Pancharatnam–Berry phase mechanism [34], the unit cell with a $\gamma = 0°$ is coded as "0." By rotating the upper metal pattern around by 90°, a "1" coding unit is obtained. The lower layer displayed in Fig. 2(c) is a square patch etched with a square ring slot. It is designed to form FSS1 and functions as a metal reflective backboard for the PBPCM. The optimal parameters of the structure are listed in Table I.

The designed PBPCM-FSS1 is simulated using CST Microwave Studio, and the result is shown in Fig. 3. Fig. 3(a) displays the reflection magnitudes exciting from Port 1. According to it, the

TABLE I
Parameters of the PBPCM-FSS1 Structure

Sizes	P_0	a_1	a_2	b_1	b_2	w_1	w_2
Value(mm)	12	0.5	1	2	4	0.1	0.19
Sizes	w_3	r_1	r_2	θ	c_1	c_2	c_3
Value(mm)	0.25	3.81	4.63	40°	12	11.5	10

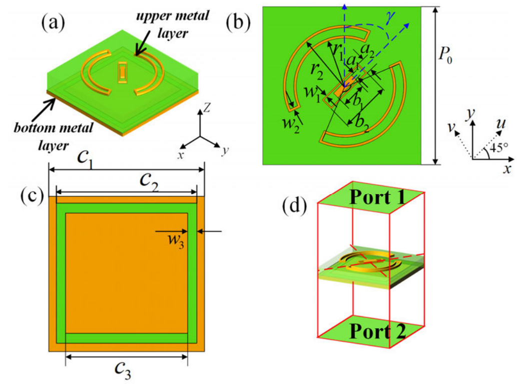

Fig. 2. Schematic of PBPCM-FSS1 structure. (a) Whole structure. (b) "0" coding unit cell. (c) FSS1 unit cell. (d) Simulation models of the whole unit cell.

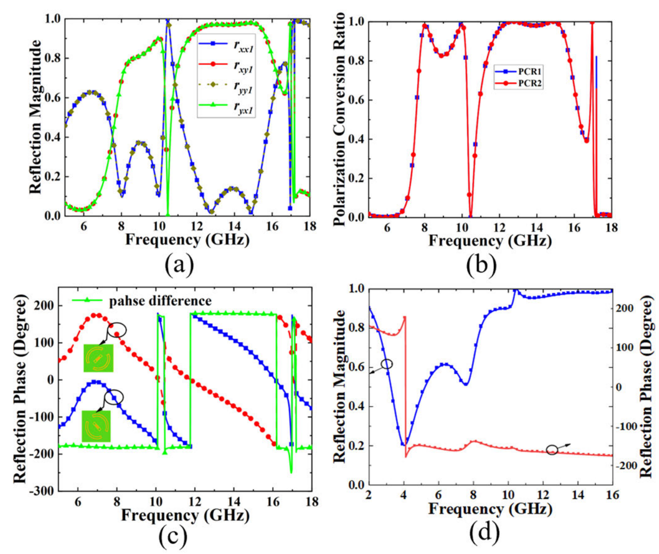

Fig. 3. Reflection coefficients of PBPCM-FSS1 structure. (a) Reflection magnitudes of coding unit cells. (b) PCR curves. (c) Cross-polarized reflection phases of coding unit cells. (d) Reflection coefficient of FSS1 unit cell.

polarization conversion ratio (PCR) can be calculated and indicated in Fig. 3(b). Here, PCR1 and PCR2 under y- and x-polarized incident waves are defined as [37]

$$PCR1 = \frac{r_{\mathrm{xy}}^2}{r_{\mathrm{xy}}^2 + r_{\mathrm{xx}}^2}, \quad PCR2 = \frac{r_{\mathrm{yx}}^2}{r_{\mathrm{yx}}^2 + r_{\mathrm{yy}}^2}. \tag{2}$$

As can be seen, the frequency bands where the "0" and "1" unit cells exhibit cross-polarization magnitudes and $PCR1/PCR2$ exceeding 0.8 are 7.78–10.3 and 11.7–15.8 GHz, respectively. Fig. 3(c) plots the cross-polarized reflection phase of the "0" and "1" unit cells. The phase difference between these two unit cells remains consistently ±180° across the entire frequency range.

In addition, Fig. 3(d) illustrates the reflection coefficient of the FSS1 unit cell when exiting from Port 2. The reflection magnitude is less than 0.3 within 3.65–4.65 GHz and exceeds 0.7 at 8.1 GHz, with a reflection phase of $-140°$. Consequently, the design is optimized for an F–P cavity antenna operation at 8.1 GHz.

B. Arrangement of PBPCM

A square metasurface consists of $M \times M$ coding elements, each with dimension D, where each element is composed of $N \times N$ “0” or “1” unit cells. Under the normal incidence of plane wave, the far-field scattering function from metasurface can be expressed as follows [34]:

$$f(\theta, \varphi) = f_e(\theta, \varphi) \sum_{m=1}^{M} \sum_{n=1}^{M} \times \exp\{-i\{\varphi(m, n) + kD \sin\theta \times [(m - 1/2)\cos\varphi + (n - 1/2)\sin\varphi]\}\} \quad (3)$$

where θ and φ represent the elevation and azimuth angles of scattering beams. The scattering phase of each element is assumed to be $\varphi(m, n)$, which is either “0” or “180.” k is the wavenumber. $f_e(\theta, \varphi)$ is the pattern function of an element, which can be equivalent to phase response of the “0” element to ensure that its relative phase is 0. The directivity function of the metasurface is given as follows [34]:

$$Dir(\theta, \varphi) = 4\pi |f(\theta, \varphi)|^2 \Big/ \int_0^{2\pi} \int_0^{\pi/2} |f(\theta, \varphi)|^2 \sin\theta d\theta d\varphi. \quad (4)$$

Therefore, the RCS reduction induced by the coding metasurface is expressed as follows [34]:

$$RCSR = \frac{\lambda^2}{4\pi N^2 D^2} MAX[Dir(\theta, \varphi)]. \quad (5)$$

According to (3)–(5), the far-field scattering characteristics are closely linked to the coding sequence of coding elements. Therefore, by modulating the coding mode of the metasurface, the direction of EM energy reflection can be altered, resulting in the diffusion of the reflected waves.

As discussed, each element is composed of $N \times N$ either “0” or “1” unit cells because the phase of coding unit cell is highly dependent on the EM coupling between unit cells. When adjacent unit cells possess different structural dimensions or direction of rotation, the reflected phase will deviate from the design value, leading to a degradation in the scattering performance of the whole metasurface.

Fig. 4(a) and (b) illustrates that when incident waves hit the “1” and “0” arrays (the phase of all coding unit cells in the coding array is the same). When the central coding unit cell in Fig. 4(a) is replaced with “0,” the reflection phase and its surrounding region change, as shown in Fig. 4(c). To ensure the desired phase response, the “0” unit cell is expanded into a 3×3 element array in a subsequent step, as shown in Fig. 4(d). Following the principle presented above, PBPCM shown in Fig. 5 is designed. It comprises 3×3 elements coding in sequence the 010/101/010. Each 0/1 element is formed from identical unit cells.

IV. Antenna Configuration for Low-Frequency Bands

A. Design and Analysis of AMC-FSS2 Structure

The whole AMC-FSS2 is displayed in Fig. 6(a). It is composed of two metal layers etched on the substrate with a thickness of 3 mm. The upper one serving as an AMC unit cell can generate a 0° reflection phase at 4.3 GHz. It is a nested polygon and square ring. The bottom layer is used as the FSS2 unit cell, which is a patch loaded a cross-slot. The optimal parameters of the structure are listed in Table II.

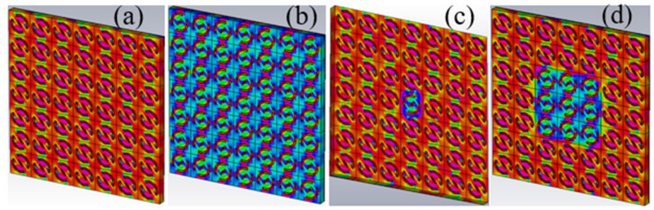

Fig. 4. Phase distribution on the coding unit cells. (a) 7 × 7 “1” coding array. (b) 7 × 7 “0” coding array. (c) Replace (a) intermediate unit in a with “0” unit cell. (d) Replace the middle 3 × 3 unit cells in (a) with a 3 × 3 “0” element.

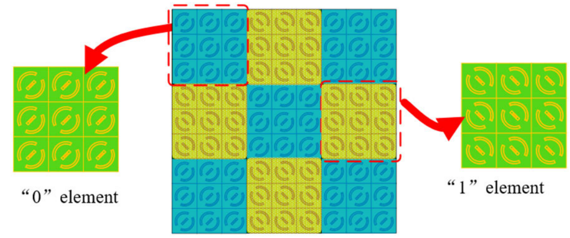

Fig. 5. Coding sequence of “0” and “1” elements.

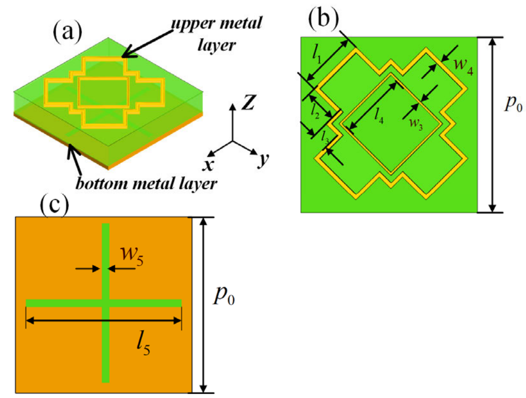

Fig. 6. Schematic of AMC-FSS2 structure. (a) Whole structure. (b) AMC unit cell. (c) FSS2 unit cell.

TABLE II
Parameters of the AMC-FSS2 Structure

Sizes	l_1	l_2	l_3	l_4	w_3	w_4	w_5	l_5
Value (mm)	4.35	2.43	1.2	5.05	0.15	0.3	0.7	11.7

Fig. 7 presents the simulation models of the AMC unit cells, and simulated reflection coefficients are shown in Fig. 8. In Fig. 8(a), the reflection magnitudes of all four structures exceed 0.8. For the AMC surface in Fig. 7(a), an operation bandwidth of 3.4–4.7 GHz is achieved, within which the reflection phase changes from +90° to −90°, with a 0° reflection phase occurring at 4.3 GHz. Also, the reflection phase of structures in Fig. 7(b) and (c) has similar characteristics. Furthermore, the height $h2$ can be reduced to $\lambda_0/4$ (λ_0 is the free space wavelength at 4.3 GHz) due to the introduction of the AMC surface with a 0° reflection phase. Therefore, the final thickness

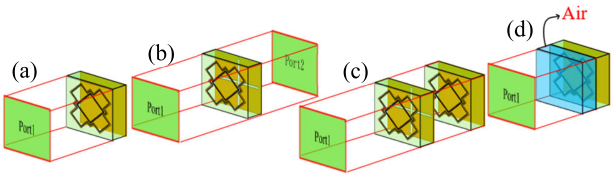

Fig. 7. Simulation models of (a) grounded AMC unit cell, (b) AMC-FSS2 unit cell, (c) AMC-FSS2-grounded AMC unit cell, and (d) air-grounded AMC unit cell.

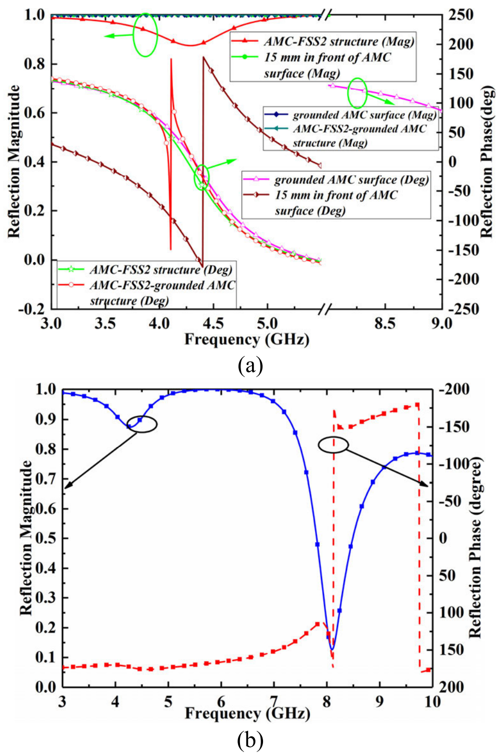

Fig. 8. Reflection coefficient of AMC and FSS2 unit cell. (a) S_{11}. (b) S_{22}.

of the air layer in Fig. 7(d) is determined to be 15 mm. Fig. 8(a) also illustrates the S_{11} of the air-grounded AMC unit cell. It shows that the cavity height causes a deviation of the reflection phase difference of 180° when comparing reflection phases of the AMC-FSS2-grounded AMC and air-grounded AMC. Therefore, a reduction of RCS is estimated because of the phase difference.

The S_{22} parameter of the AMC-FSS2 unit cell shown in Fig. 8(b) exhibits a reflection magnitude of less than 0.3 in the range of 7.8–8.4 GHz and greater than 0.8 at 4.3 GHz, and the reflection phase is –178°. Consequently, an F–P cavity antenna working at 4.3 GHz is achieved. Especially, the h_1 is calculated to be 23.25 mm according to the reflection phases of FSS1 and the AMC plane.

B. AMC Surfaces Configuration for Middle and Bottom Layers

At low frequencies, the incident waves are reflected by the middle and bottom layers into two components, denoted as a and b. The corresponding reflected electric fields are E_{a} and E_{b}, with reflection phases φ_{a} and φ_{b} and reflection magnitudes A_{a} and A_{b}, respectively. To minimize the total reflected electric field, the sum of the E_{a} and E_{b} must equal to zero. This condition requires that A_{a} and A_{b} are equal, while φ_{a} and φ_{b} are in opposite phases. As analyzed in Section IV-A, φ_{a} and φ_{b} correspond to the reflection phases of the structures in Fig. 7(c) and (d), respectively, with $\varphi_{\mathrm{a}} = 0°$ and $\varphi_{\mathrm{b}} = 180°$. It can be concluded in Fig. 9 that the number of unit cells in the middle layer should be half of the number in the bottom layer. This ensures that A_{a} and A_{b} are equal, contributing to the strength cancellation of E_{a} and E_{b}. Consequently, RCS reduction at low frequencies can be achieved by incorporating the AMC-FSS2 and AMC structure.

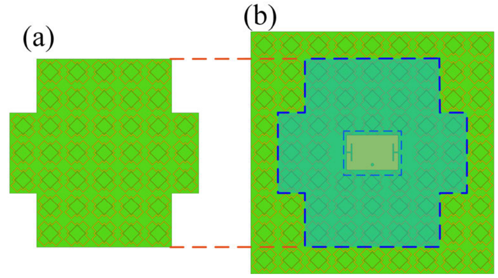

Fig. 9. Top view of the middle and the bottom layers of the proposed antenna. (a) Middle layer. (b) Bottom layer.

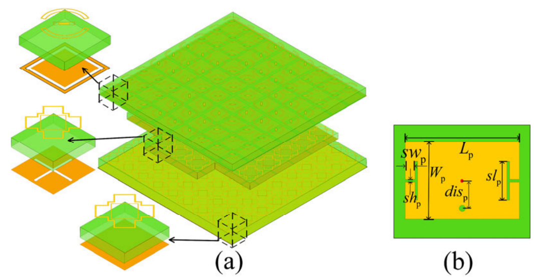

Fig. 10. (a) Proposed F–P cavity antenna. (b) Feed source.

TABLE III
STRUCTURAL PARAMETERS OF THE PATCH ANTENNA

Sizes	L_{p}	W_{p}	sw_{p}	sh_{p}	dis_{p}	sl_{p}
Value(mm)	23	17.5	2	0.5	3.25	7.2

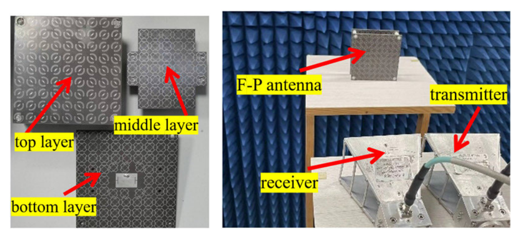

Fig. 11. Prototype of the proposed antenna and test setup.

V. DESIGN AND MEASUREMENT OF LOW-RCS ANTENNA

A. Reference Antenna and Proposed Antenna

Based on the results in Sections III and IV, the whole F–P cavity antenna and radiation source are designed, and its structure is shown in Fig. 10. Here, $h = 30$ mm. A patch antenna (its dimensions are listed in Table III) etched with two T-shaped slots on the non-radiating edges is selected as the radiation source. Also, it is used as a reference antenna when exhibiting the RCS reduction performance of the proposed antenna.

B. Measured and Simulated Scattering Performance

Fig. 11 shows the prototype of the F–P cavity antenna and the corresponding test setup. The simulated monostatic RCS, as well as RCS reduction of the reference and proposed antennas under

TABLE IV
COMPARISON BETWEEN THE PROPOSED DESIGN AND SEVERAL REPORTED LOW-RCS F–P CAVITY ANTENNAS

References	Impedance bandwidth (GHz)	RCS-reduction bandwidth (GHz)	Gain (dBi)	Total profile (mm)
[5]	11.2~11.62 (3.7%)	6~14 (80%)	13.5	14.7 (0.38λ_0)
[22]	8.36~8.46 (1.2%)	7~11 (44%)	17.9	24 (0.67λ_0)
[23]	6.05~6.72 (10.4%)	5.5~7 (24%)	10	41 (0.87λ_0)
[28]	9.46~11.34 (18%)	8~18 (77%)	12.1	17 (0.57λ_0)
This work	4.15-4.80 (14.5%) 7.8-8.4 (7.4%)	3~16 (136.8%)	10, 15.9	18 (0.21λ_0), 34 (0.71λ_0)

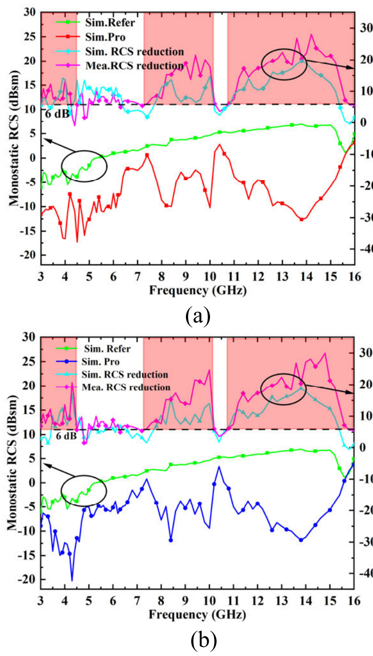

Fig. 12. Measured and simulated monostatic RCS and RCS reduction of both antenna under (a) x-polarized and (b) y-polarized incident waves.

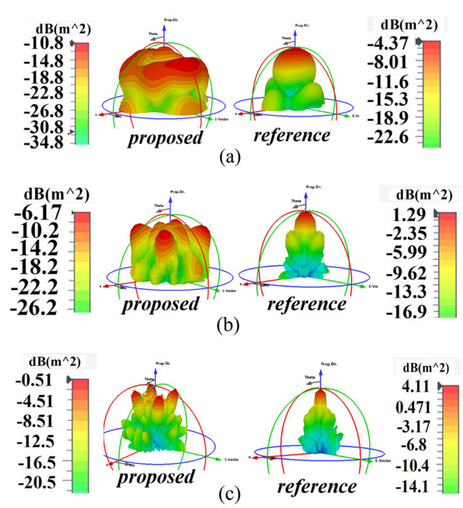

Fig. 13. Three-dimensional patterns of bistatic scattering of the proposed F–P cavity antenna and the reference antenna at (a) 4.3 GHz. (b) 8.5 GHz. (c) 14 GHz.

x-polarized and y-polarized incident waves, are both depicted in Fig. 12. It indicates a significant suppression of backward RCS across a wide frequency band ranging from 3 to 16 GHz, and the 6-dB RCS reduction bandwidths are 3–4.8 GHz, 7.2–10.2 GHz, 10.8–16 GHz, covering two working frequency bands for both polarization cases.

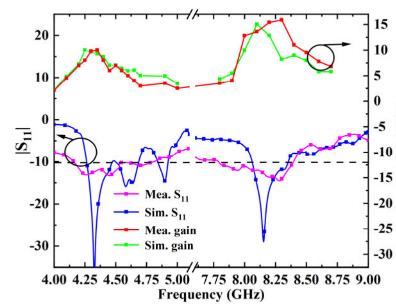

Fig. 14. Measured and simulated reflection coefficients and peak gains of F–P cavity antenna.

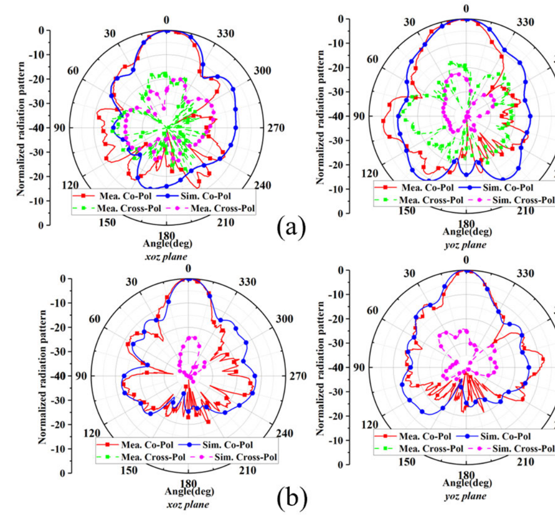

Fig. 15. Measured and simulated normalized radiation patterns of F–P cavity antenna in (a) 4.3 GHz and (b) 8.1 GHz.

Additionally, the 3-D scattering patterns at 4.3, 8.5, and 14 GHz under x polarization are illustrated in Fig. 13. It can be observed that the backward scattering waves are redirected to more directions.

C. Measured and Simulated Radiation Performance

Fig. 14 illustrates the simulated and measured S_{11} and peak gain. The -10 dB impedance bandwidth of the realized antenna is in the range of 4.15–4.80 GHz and 7.8–8.4 GHz. The maximum gain is 10 dBi at 4.35 GHz and 15.9 dBi at 8.3 GHz. According to the equation in [36], the aperture efficiency of the proposed antenna in the two frequency bands is 17.3% (f = 4.45 GHz) and 47.1% (f = 8.3 GHz), respectively. The radiation patterns are plotted in

Fig. 15. A good agreement between simulation and measurement can be observed. In particular, the cross-polarization is more than 20 dB lower than the co-polarization in the main radiation direction.

Finally, a performance comparison between the proposed antenna and previously published works is listed in Table IV. It shows that the proposed antenna exhibits an ultra-wide RCS reduction bandwidth and can operate in dual frequency bands.

VI. Conclusion

This communication presents a combination of two methods for reducing RCS, applied to a dual-band F–P cavity antenna with low RCS over a wide frequency range. By integrating coding metasurfaces, AMC structures, and two FSS layers, the antenna simultaneously achieves low backward scattering and dual-band operation. The design and operational principles of the F–P cavity antenna and RCS reduction are discussed in detail. The proposed F–P cavity antenna has an improved radiation pattern and enhanced gain in the frequency bands of 4.15–4.80 and 7.8–8.4 GHz, with an RCS reduction bandwidth ranging from 3 to 16 GHz. The measured results have verified the feasibility of the design method. This integrated approach offers a novel pathway for achieving wideband RCS reduction in a multiband F–P cavity antenna.

References

[1] M. S. Rabbani, J. Churm, and A. P. Feresidis, "Fabry–Pérot beam scanning antenna for remote vital sign detection at 60 GHz," *IEEE Trans. Antennas Propag.*, vol. 69, no. 6, pp. 3115–3124, Jun. 2021.

[2] M. S. Rabbani and H. Ghafouri-Shiraz, "Frequency selective surface antenna for remote vital sign monitoring with ultra-wide band Doppler radar," *Microw. Opt. Technol. Lett.*, vol. 59, no. 4, pp. 818–823, Apr. 2017.

[3] A. Goudarzi, M. M. Honari, and R. Mirzavand, "A millimeter-wave Fabry–Pérot cavity antenna with unidirectional beam scanning capability for 5G applications," *IEEE Trans. Antennas Propag.*, vol. 70, no. 3, pp. 1787–1796, Mar. 2022.

[4] F. Qin et al., "Wideband circularly polarized Fabry–Pérot antenna," *IEEE Antennas Propag. Mag.*, vol. 57, no. 5, pp. 127–135, Nov. 2015.

[5] W. Pan, C. Huang, P. Chen, X. Ma, C. Hu, and X. Luo, "A low-RCS and high-gain partially reflecting surface antenna," *IEEE Trans. Antennas Propag.*, vol. 62, no. 2, pp. 945–949, Feb. 2014.

[6] R. Gardelli, M. Albani, and F. Capolino, "Array thinning by using antennas in a Fabry–Pérot cavity for gain enhancement," *IEEE Trans. Antennas Propag.*, vol. 54, no. 7, pp. 1979–1990, Jul. 2006.

[7] Y. Liu, L. Xu, X. Zhao, J. Zhang, S. Wang, and W. Zhang, "A dual-band low-profile Fabry–Pérot resonator antenna with single partially reflecting surface," *Electromagnetics*, vol. 43, no. 7, pp. 492–505, Oct. 2023.

[8] Y. F. Liu et al., "Design of a wideband Fabry–Pérot resonator antenna with a double-layer partially reflective surface," *Int. J. RF Microw. Comput.-Aided Eng.*, vol. 32, no. 12, Oct. 2022, Art. no. e23489.

[9] N. Wang, Q. Liu, C. Wu, L. Talbi, Q. Zeng, and J. Xu, "Wideband Fabry–Pérot resonator antenna with two complementary FSS layers," *IEEE Trans. Antennas Propag.*, vol. 62, no. 5, pp. 2463–2471, May 2014.

[10] K. Konstantinidis, A. P. Feresidis, and P. S. Hall, "Dual subwavelength Fabry–Pérot cavities for broadband highly directive antennas," *IEEE Antennas Wireless Propag. Lett.*, vol. 13, pp. 1184–1186, 2014.

[11] R. Orr, G. Goussetis, and V. Fusco, "Design method for circularly polarized Fabry–Pérot cavity antennas," *IEEE Trans. Antennas Propag.*, vol. 62, no. 1, pp. 19–26, Jan. 2014.

[12] Z.-G. Liu and W.-B. Lu, "Low-profile design of broadband high gain circularly polarized Fabry–Pérot resonator antenna and its array with linearly polarized feed," *IEEE Access*, vol. 5, pp. 7164–7172, 2017.

[13] P. Xie, G. Wang, H. Li, J. Liang, and X. Gao, "Circularly polarized Fabry–Pérot antenna employing a receiver–transmitter polarization conversion metasurface," *IEEE Trans. Antennas Propag.*, vol. 68, no. 4, pp. 3213–3218, Apr. 2020.

[14] X. Yang, Y. Liu, H. Lei, Y. Jia, P. Zhu, and Z. Zhou, "A radiation pattern reconfigurable Fabry–Pérot antenna based on liquid metal," *IEEE Trans. Antennas Propag.*, vol. 68, no. 11, pp. 7658–7663, Nov. 2020.

[15] R. Lian, Z. Tang, and Y. Yin, "Design of a broadband polarization-reconfigurable Fabry–Pérot resonator antenna," *IEEE Antennas Wireless Propag. Lett.*, vol. 17, pp. 122–125, 2018.

[16] M. Li et al., "A millimeter-wave frequency-reconfigurable Fabry–Pérot cavity antenna," *IEEE Antennas Wireless Propag. Lett.*, vol. 21, pp. 1537–1541, 2022.

[17] Y.-H. Lv, X. Ding, and B.-Z. Wang, "Dual-wideband high-gain Fabry–Pérot cavity antenna," *IEEE Access*, vol. 8, pp. 4754–4760, 2020.

[18] J. Qi, Q. Wang, F. Deng, Z. Zeng, and J. Qiu, "Low-profile unicavity high-gain FPC antenna covering entire global 2.4 GHz and 5 GHz WiFi-bands using uncorrelated dual-band PRS and phase compensation AMC," *IEEE Trans. Antennas Propag.*, vol. 70, no. 11, pp. 10187–10198, Nov. 2022.

[19] Z.-G. Liu, R.-J. Yin, Z.-N. Ying, W.-B. Lu, and K.-C. Tseng, "Dual-band and shared-aperture Fabry–Pérot cavity antenna," *IEEE Antennas Wireless Propag. Lett.*, vol. 20, pp. 1686–1690, 2021.

[20] F. Qin et al., "A triband low-profile high-gain planar antenna using Fabry–Pérot cavity," *IEEE Trans. Antennas Propag.*, vol. 65, no. 5, pp. 2683–2688, May 2017.

[21] H. Jiang, Z. Xue, W. Li, W. Ren, and M. Cao, "Low-RCS high-gain partially reflecting surface antenna with metamaterial ground plane," *IEEE Trans. Antennas Propag.*, vol. 64, no. 9, pp. 4127–4132, Sep. 2016.

[22] Y. Jia, Y. Liu, W. Zhang, J. Wang, S. Gong, and G. Liao, "High-gain Fabry–Pérot antennas with wideband low monostatic RCS using phase gradient metasurface," *IEEE Access*, vol. 7, pp. 4816–4824, 2019.

[23] J. Zhang, Y. Liu, Y. Jia, and R. Zhang, "High-gain Fabry–Pérot antenna with reconfigurable scattering patterns based on varactor diodes," *IEEE Trans. Antennas Propag.*, vol. 70, no. 2, pp. 922–930, Feb. 2022.

[24] Z. Luo, X. Ren, Q. Wang, Q. Cheng, and T. Cui, "Anisotropic and nonlinear metasurface for multiple functions," *Sci. China Inf. Sci.*, vol. 64, no. 9, Sep. 2021, Art. no. 192301.

[25] Z. Luo et al., "Active metasurface absorber for intensity-dependent surface-wave shielding," *IEEE Trans. Antennas Propag.*, vol. 71, no. 7, pp. 5795–5804, Jul. 2023.

[26] Z. Luo et al., "Fully breaking entanglement of multiple harmonics for space- and frequency-division multiplexing wireless applications via space-time-coding metasurface," *Adv. Sci.*, vol. 11, no. 34, Jul. 2024, Art. no. 2404558.

[27] M. Long, W. Jiang, and S. Gong, "Wideband RCS reduction using polarization conversion metasurface and partially reflecting surface," *IEEE Antennas Wireless Propag. Lett.*, vol. 16, pp. 2534–2537, 2017.

[28] Y. Zheng et al., "Wideband gain enhancement and RCS reduction of Fabry–Pérot resonator antenna with chessboard arranged metamaterial superstrate," *IEEE Trans. Antennas Propag.*, vol. 66, no. 2, pp. 590–599, Feb. 2018.

[29] L. Zhang et al., "Realization of low scattering for a high-gain Fabry–Pérot antenna using coding metasurface," *IEEE Trans. Antennas Propag.*, vol. 65, no. 7, pp. 3374–3383, Jul. 2017.

[30] J. Ren, W. Jiang, K. Zhang, and S. Gong, "A high-gain circularly polarized Fabry–Pérot antenna with wideband low-RCS property," *IEEE Antennas Wireless Propag. Lett.*, vol. 17, pp. 853–856, 2018.

[31] S. Zarbakhsh, M. Akbari, F. Samadi, and A.-R. Sebak, "Broadband and high-gain circularly-polarized antenna with low RCS," *IEEE Trans. Antennas Propag.*, vol. 67, no. 1, pp. 16–23, Jan. 2019.

[32] C. Huang, W. Pan, X. Ma, and X. Luo, "A frequency reconfigurable directive antenna with wideband low-RCS property," *IEEE Trans. Antennas Propag.*, vol. 64, no. 3, pp. 1173–1178, Mar. 2016.

[33] Q.-Y. Guo and H. Wong, "Wideband and high-gain Fabry–Pérot cavity antenna with switched beams for millimeter-wave applications," *IEEE Trans. Antennas Propag.*, vol. 67, no. 7, pp. 4339–4347, Jul. 2019.

[34] T. J. Cui, M. Q. Qi, X. Wan, J. Zhao, and Q. Cheng, "Coding metamaterials, digital metamaterials and programmable metamaterials," *Light, Sci. Appl.*, vol. 3, no. 10, p. e218, Oct. 2014.

[35] C. Fu, L. Han, C. Liu, X. Lu, and Z. Sun, "Combining Pancharatnam–Berry phase and conformal coding metasurface for dual-band RCS reduction," *IEEE Trans. Antennas Propag.*, vol. 70, no. 3, pp. 2352–2357, Mar. 2022.

[36] Y.-F. Cheng, L. Yang, X. Zhong, C. Liao, and X. Ding, "Analysis and design of wideband low-RCS Fabry–Pérot antennas with reduced profile," *IEEE Trans. Antennas Propag.*, vol. 70, no. 9, pp. 7934–7943, Sep. 2022.

[37] X. Huang, H. Yang, D. Zhang, and Y. Luo, "Ultrathin dual-band metasurface polarization converter," *IEEE Trans. Antennas Propag.*, vol. 67, no. 7, pp. 4636–4641, Jul. 2019.